

LETTER • OPEN ACCESS

## Active particles with delayed attractions form quaking crystallites<sup>(a)</sup>

To cite this article: Pin-Chuan Chen *et al* 2023 *EPL* **142** 67003





View the [article online](#) for updates and enhancements.

You may also like

- [Sufficient sampling for kriging prediction of cortical potential in rat, monkey, and human uECoG](#)  
Michael Trumpis, Chia-Han Chiang, Amy L Orsborn et al.
- [The bioengineering of perfusable endocrine tissue with anastomosing blood vessels](#)  
Hiroki Yago, Jun Homma, Hidekazu Sekine et al.
- [Transcription and logic operations of magnetic skyrmions in bilayer cross structures](#)  
Kai Yu Mak, Jing Xia, Xichao Zhang et al.

Focus Article

# Active particles with delayed attractions form quaking crystallites<sup>(a)</sup>

PIN-CHUAN CHEN<sup>1(b)</sup> , KLAUS KROY<sup>1(c)</sup> , FRANK CICHOS<sup>2(d)</sup> , XIANGZUN WANG<sup>2(e)</sup>  
and VIKTOR HOLUBEC<sup>3(f)</sup> 

<sup>1</sup> *Institute for Theoretical Physics, Universität Leipzig - 04103 Leipzig, Germany*

<sup>2</sup> *Molecular Nanophotonics Group, Peter Debye Institute for Soft Matter Physics, Universität Leipzig 04103 Leipzig, Germany*

<sup>3</sup> *Department of Macromolecular Physics, Faculty of Mathematics and Physics, Charles University 18000 Prague, Czech Republic*

received 1 March 2023; accepted in final form 30 May 2023  
published online 13 June 2023

**Abstract** – Perception-reaction delays have experimentally been found to cause a spontaneous circling of microswimmers around a fixed target particle. Here we investigate a many-body version of such an experiment with Brownian-dynamics simulations of active particles in a plane. For short delays, they form a hexagonal crystallite around the target. The bifurcation to a chiral dynamical phase, seen for longer delays, maps onto that for a single active particle. Different angular velocities at different distances from the target induce shear stresses that grow with increasing delay. By exciting shear bands, they shake and intermittently break the rotating crystallite. For long delays, it detaches from the target to circle around it near the preferred single-particle orbit as a compact spinning satellite, trembling from what could be called tidal quakes.

 open access

 focus article

Copyright © 2023 The author(s)

Published by the EPLA under the terms of the [Creative Commons Attribution 4.0 International License](https://creativecommons.org/licenses/by/4.0/) (CC BY). Further distribution of this work must maintain attribution to the author(s) and the published article's title, journal citation, and DOI.

**Introduction.** – Recent experiments with synthetic microswimmers steered toward a fixed target have revealed a spontaneous vortex formation caused by a perception-reaction delay [1]. The observed phenomenology can be attributed to the delay-induced aiming errors, akin to those associated with microswimmer navigation strategies employing “vision-cone” [2,3] or “acceptance-angle” [4,5] criteria. The experiment thereby established a simple paradigmatic model system for swarm forming ensembles with delayed interactions. Notably, the reaction of all living creatures and artificial devices to external stimuli is delayed by the time required to transfer and process information and realize the required response. All these systems can be classified as feedback-driven systems [6],

which are well studied in control theory, a branch of dynamical-systems theory. In physics, objects capable of an active response to perceived stimuli, such as animals or robots, are commonly studied within the field of active matter [7]. Even though most models of active matter neglect perception-reaction delays, it was shown that delays can significantly impact stability, dynamical phases, and even finite-size scaling in active matter systems [8–16].

In this letter, we numerically study a model system introduced and experimentally motivated in ref. [1]. We extend the analysis to particle numbers that are currently inaccessible to the experimental techniques [17] employed. Using Brownian-dynamics simulations, we find that the average angular velocity still exhibits the bifurcation described for small particle numbers in ref. [1], but that the many-body dynamics undergoes a surprisingly rich series of delay-induced dynamical phase transitions. For short delays, a densely packed crystallite forms around the target. The mechanism somewhat resembles motility-induced phase separation [18], in the sense that the clusters are maintained by swim forces in a strongly depleted

<sup>(a)</sup>Contribution to the Focus Issue *Statistical Physics of Self-Propelled Colloids* edited by Hartmut Löwen, Sabine Klapp and Holger Stark.

<sup>(b)</sup>E-mail: eddyedward0427@gmail.com (corresponding author)

<sup>(c)</sup>E-mail: klaus.kroy@uni-leipzig.de

<sup>(d)</sup>E-mail: cichos@physik.uni-leipzig.de

<sup>(e)</sup>E-mail: wangxiangzun@gmail.com

<sup>(f)</sup>E-mail: viktor.holubec@mff.cuni.cz

gas phase. As the delay increases, the crystallite is intermittently broken up by delay-induced shear bands.

Even for experimentally realistic noise intensities, the phenomenology observed in our simulations resembles the behavior of sheared low-temperature colloidal suspensions or athermal granular materials [19,20]. An important feature of densely packed crystalline and amorphous particle assemblies is that they can only be sheared if the packing structure is somewhat dilated to allow the particles to escape from their nearest-neighbor cages and move around each other. Typical defect structures observed under such conditions are therefore shear bands [21,22]. In the field of granular rheology, one also speaks of the dilatancy effect. It is responsible for normal stresses and the non-affine response to shear. In everyday life, you may experience it in the form of drained halos around your feet when you step on wet sand. In contrast to common granular and colloidal rheological setups, the shear stresses in our active-Brownian-particle ensembles are however not induced by a moving background solvent or a system boundary or immersed probe particle, but solely by the individual particles' activity itself. This entails some counter-intuitive consequences. Most importantly, the time delay only entails relevant navigational aiming errors if the particles are actually moving, but not if they are jammed up in a dense cluster. This somewhat unconventional property distinguishes our setup from the myriad of superficially related rheological problems documented in the literature. It also impedes attempts to provide a complete mechanistic interpretation of the unique succession of dynamical phases and phase transitions, described in the following.

**Model.** – We consider a two-dimensional system of  $N$  overdamped active Brownian discs, interacting via soft steric interactions. One particle is held fixed at the origin. The  $N$  mobile particles aim to move toward it with a constant speed  $v_0$ . As shown in fig. 1(a), they cannot react instantaneously to the detected target position, but only after a certain delay time  $\delta t$ . Since the particles keep moving during this time, the resulting retarded attraction to the central target acquires important aiming errors.

We fix length and time scales by setting the particle diameter and the speed to unity (*i.e.*, the time unit is particle diameter over speed; see table S1 in the Supplementary Material [SupplementaryMaterial.pdf](#) (SM)). The dimensionless position vector  $\mathbf{r}_i$  of the  $i$ -th Brownian particle at the dimensionless time  $t$  obeys the Langevin equation

$$\dot{\mathbf{r}}_i(t) = \mathbf{F}_i(t) + k \sum_{j \neq i} \mathbf{r}_{ij}(t) \Theta[1 - |\mathbf{r}_{ij}(t)|] + \sqrt{2D} \boldsymbol{\eta}_i(t), \quad (1)$$

where  $\mathbf{F}_i(t) = -\mathbf{r}_i(t - \delta t)/|\mathbf{r}_i(t - \delta t)|$  are the “intended” nominal velocities of the individual particles, which differ from the actual velocities  $\dot{\mathbf{r}}_i$ , due to inter-particle interactions and noise. The soft steric repulsion has a strength given by the dimensionless stiffness  $k$  and a range cut-off at  $|\mathbf{r}_{ij}(t)| = 1$  (the “particle diameter”), imposed by the Heaviside  $\Theta$  function. The diffusivity  $D$  controls the

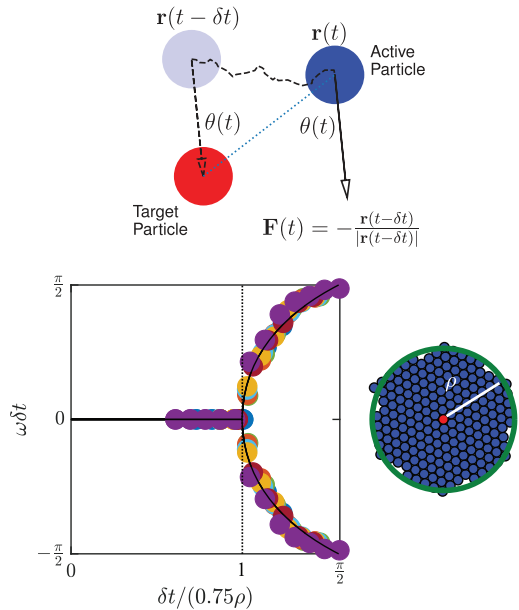


Fig. 1: Active Brownian particles (blue), moving at constant speed, aim at a central target (red) with a perception-reaction delay  $\delta t$ . (a) the fact that the actual direction of motion at time  $t$  is determined by position  $\mathbf{r}(t - \delta t)$  at the earlier time  $t - \delta t$  gives rise to aiming errors and ensuing dynamical phases. (b) The bifurcation diagram shows the average angular displacement  $\omega \delta t$  per delay time  $\delta t$ . Upon increasing delay, the isotropic static phase (I) gives way to radially symmetric chiral phases (II–IV). For the yin-yang and blob phases (V and VI),  $\omega \delta t \approx \pi/2$ . The colors code for various particle numbers  $N = 30, \dots, 1000$ . The diagram obtained for athermal motion (diffusivity  $D = 0$ ) remains unchanged for an experimentally realistic noise intensity ( $D = 0.0136$ ). (c) Close-packed crystallites of  $N \gtrsim 30$  particles have radius  $\rho = \sqrt{(N + 1)}/3.62$  in units of the (soft-)particle diameter.

intensity of mutually independent Gaussian white noise vectors  $\boldsymbol{\eta}_i$ ,  $i = 1, \dots, N$ , with zero mean,  $\langle \boldsymbol{\eta}_i(t) \rangle = \mathbf{0}$ , and covariance  $\langle [\boldsymbol{\eta}_i(t)]_x [\boldsymbol{\eta}_j(t')]_y \rangle = \delta_{ij} \delta_{xy} \delta(t - t')$ , where  $[\boldsymbol{\eta}_i(t)]_x$  denotes the  $x$  component of vector  $[\boldsymbol{\eta}_i]$ . We do not consider rotational diffusion, as it is irrelevant for the experimental setup in ref. [1], which motivated our work.

We studied for particle numbers  $N = 15, \dots, 1000$  that are neither analytically tractable nor currently realizable in experiments. The dynamical equations are solved by Brownian-dynamics simulations with time step 0.001, stiffness  $k = 101.4$ , and diffusion coefficient  $D = 0.0136$ . The chosen value for the diffusion coefficient corresponds to typical experimental conditions in aqueous solvents at room temperature, if the particle diameter is identified with  $2.19 \times 10^{-6}$  m and the propulsion speed with  $2.16 \times 10^{-6}$  m/s [1]. We initialized the particles randomly around the origin, let them diffuse for a time  $t = \delta t$ , and simulated long enough such that the system relaxed to a steady state (see the Supplementary Videos [VideoS1.mp4](#), [VideoS2.mp4](#), [VideoS3.mp4](#), [VideoS4.mp4](#), [VideoS5.mp4](#), [VideoS6.mp4](#), [VideoS7.mp4](#), [VideoS8.mp4](#), [VideoS9.mp4](#),

VideoS10.mp4 (SV)). Afterward, we continued the simulation and collected the data. Varying  $k$  and  $D$  in the dynamical equations (1) within an experimentally reasonable range does not change the qualitative results. (For better visibility of the structural differences, we have chosen to only show results for zero diffusivity,  $D = 0$ , in the main figures, but see supplementary videos VideoS7.mp4 and VideoS10.mp4) Hence, the relevant control parameters are the time delay  $\delta t$  and particle number  $N$ , or the corresponding radius  $\rho(N) \equiv \sqrt{(N+1)}/3.62$  of a close packed hexagonal crystallite (see fig. 1(c)).

**Bifurcation.** – As shown in ref. [1], for  $N = 1$ , the average angular velocity  $\omega$  of the single active Brownian particle around the fixed target is determined by a transcendental self-consistency equation. If the active-particle and target diameters are set to unity, it takes the form of the “sine map”  $\omega = \sin(\omega\delta t)$ . It exhibits a bifurcation from  $\omega = 0$  to  $\omega \neq 0$  at  $\delta t = 1$  (or, in the dimensional units of ref. [1],  $v_0\delta t = 2a$ ). For  $1 < \delta t < \pi/2$ , the single active Brownian particle “slides” around the target, and thus its dimensionless orbit radius is close to 1. When  $\delta t > \pi/2$ , the active and target particle lose contact and the circular orbit “takes off”. Its radius  $R = 2\delta t/\pi$  is now determined by the condition that the angular displacement of the particle per one delay time,  $\omega\delta t$ , is  $\pi/2$ . In other words, for large delay times, the particle always propels tangentially (at a right angle) to the target, corresponding to a self-selected circular orbit (optimal single-particle orbit).

Though not accessible experimentally, ref. [1] already demonstrated by Brownian-dynamics simulations that the single-particle bifurcation diagram stays meaningful for many particles up to  $N = 100$ . The increased particle number actually stabilizes the spontaneously chosen sense of rotation against Brownian fluctuations, rendering the transient chiral symmetry breaking quasi permanent. More importantly, the increase in particle number merely renormalizes the bifurcation diagram. As shown in fig. 2(b), the average angular particle displacement  $\omega\delta t$  around the fixed target particle for  $N$  ranging from 30 to 1000 indeed falls on a single master curve, if plotted against  $\delta t/(0.75\rho)$ , corresponding to the renormalized sine map  $0.75\rho\omega = \sin(\omega\delta t)$ . The bifurcation curve coincides with that of a single large quasi-particle of radius  $(0.75\rho - 0.5)$ , rotating around the target particle of radius 0.5. In other words, the minimum radius for active rotation (originally given by the particle diameter) equals  $0.75\rho$ , in the many-body case. One can speculate that the effective radius  $0.75\rho$  could coincide with the crystallite’s radius of gyration  $\int_0^\rho dx 2\pi x^2/(\pi\rho^2) \approx 0.67\rho$ . This is indeed not far off, although the data is more suggestive of a matching of the radius  $R = 2\delta t/\pi$  of the optimal single-particle orbit with  $\rho/2$ . This could suggest that spinning starts when the preferred nominal velocity components of the particles inside and outside the optimal orbit cancel out. The difficulty with such interpretation is that the actually measured nominal velocity field created by the

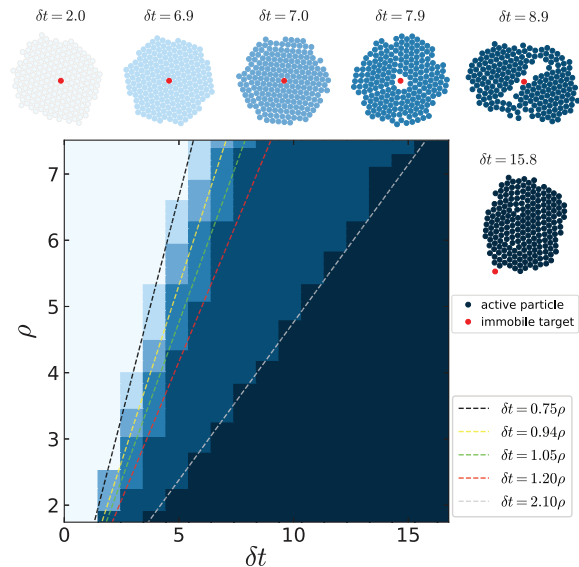


Fig. 2: Dynamic phase diagram. Like the preferred single-particle orbit  $R$ , the (binned) crystallite radius  $\rho$  grows with increasing delay time  $\delta t$ . We distinguish phases with a (I) static, (II) spinning, and (III) quaking crystallite, and a (IV) ring, (V) yin-yang/blobs, and (VI) satellite, respectively. Notice the appearance of predominantly concentric (III), radial (IV) and criss-crossing (V-VI) shear bands that intermittently break the crystallite, giving rise to a staircase-like increase of the shear strain  $\Gamma(t)$  (3rd row of fig. 3), for all but the first two phases.

highly frustrated active particles in the bulk of a solid crystallite is, for the relevant delays, still purely central.

As shown in fig. 2 for particle numbers  $N = 15, \dots, 200$ , when the delay time  $\delta t$  is increased, the particle ensemble experiences a series of abrupt dynamical changes, thereby evolving from a static hexagonal crystallite to a continuously breaking elliptic satellite droplet, circling around the target on an orbit close to that preferred by a single active particle. Remarkably, the average angular velocity in all these phases obeys the effective single-particle theory well. In fact, the single-particle theory can be used as a starting point for understanding most of the features of the various dynamical phases of the many-body model.

**Order parameters.** – To distinguish between the six dynamical phases in fig. 2, we introduce the following three order parameters:

- the radial distribution  $p(r)$  (the probability density to find an active particle at distance  $r$  from the targeted center), normalized as  $2\pi \int_0^\infty dr r p(r) = 1$ .
- the absolute value  $\omega(r) \equiv r^{-2} |\langle \mathbf{r}_i \times \dot{\mathbf{r}}_i \rangle_{|\mathbf{r}_i| \approx r}|$  of the angular velocity. (The average was evaluated over concentric shells of width 0.14.)
- the cumulative shear strain  $\Gamma(t) = \int_0^t dt' |\dot{\Gamma}(t')|$  around a representative bulk particle at time  $t$ . Formally, the shear rate is defined as  $\dot{\Gamma} = (\partial v_x / \partial y + \partial v_y / \partial x) / 2$ , where  $v_{x,y}$  denote Cartesian components of the velocity field. As a

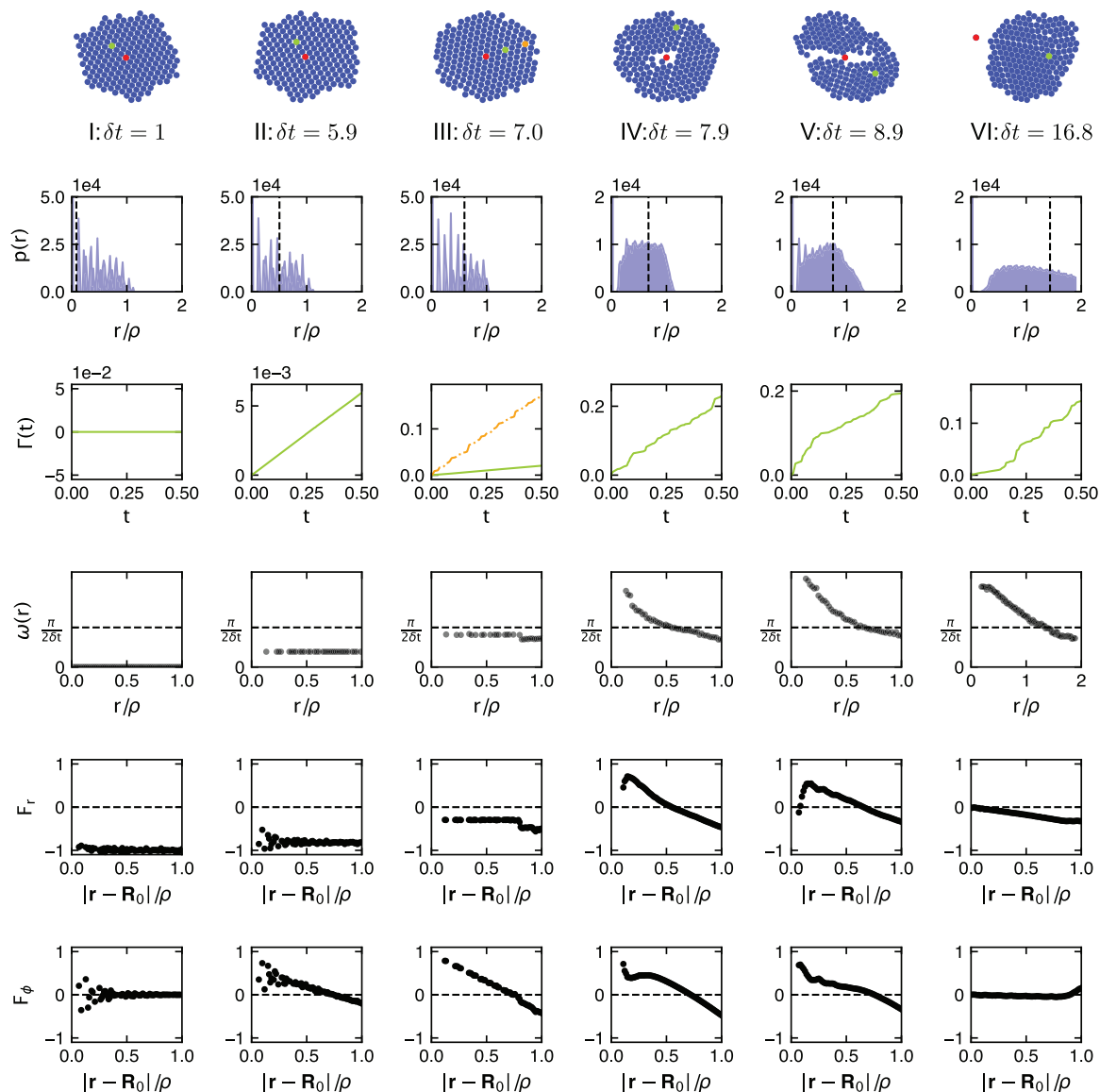


Fig. 3: Crystallite configurations and their shell angular velocities  $\omega(r)$  and the accumulated shear strains  $\Gamma(t)$  for selected bulk particles (green and orange), as caused by the radial and tangential “forces” or nominal swim velocities  $F_r, F_\phi$  in the co-moving, co-spinning frame. The corresponding force fields are shown in the SM, fig. S1. The dynamical phases I to VI of fig. 2 were simulated for vanishing thermal noise  $D = 0$  and  $N = 199$  particles (corresponding to  $\rho \approx 7.43$  if close-packed). Vertical dashed lines in the radial distribution functions  $p(r)$  indicate the preferred single particle orbit radius  $R = 2\delta t/\pi$ .

proxy for our particulate system, we use

$$\dot{\Gamma}(t) = \frac{1}{2} \sum_j \left( \frac{\dot{x}_i(t) - \dot{x}_j(t)}{y_i(t) - y_j(t)} + \frac{\dot{y}_i(t) - \dot{y}_j(t)}{x_i(t) - x_j(t)} \right). \quad (2)$$

The sum runs over nearest-neighbor shell particles  $j$  that are less than  $\sqrt{2}$  away from a selected bulk particle  $i$ . To obtain the time derivatives of the components  $x_i(t)$  and  $y_i(t)$  of the position vector  $\mathbf{r}_i(t)$ , we average eq. (1) over 200 simulation time steps. Spurious coordinate singularities are regularized by discarding terms with denominators smaller than 0.05.

**Dynamical phases.** – As shown in fig. 3, each of the dynamical phases differs from the other five either in

the topology of the cluster or in the qualitative behavior of at least one of the characteristics  $p(r)$ ,  $\omega(r)$ , and  $\Gamma(t)$ . The figure also shows the average radial and tangential projections of the nominal velocities (or “forces”)  $\mathbf{F}_i - \dot{\mathbf{R}}_0$  of particles in the co-moving frame at a given distance from the center of mass  $\mathbf{R}_0 = \sum_{i=1}^N \mathbf{r}_i/N$  of the system. The average radial projection  $F_r(r) \equiv \langle (\mathbf{F}_i - \dot{\mathbf{R}}_0) \cdot (\mathbf{r}_i - \mathbf{R}_0)/r \rangle_{|\mathbf{r}_i - \mathbf{R}_0| \approx r}$  can be interpreted as a “shell pressure”. In the depicted average tangential component  $F_\phi(r) \equiv \langle |(\mathbf{F}_i - \dot{\mathbf{R}}_0) \times (\mathbf{r}_i - \mathbf{R}_0)/r| \rangle_{|\mathbf{r}_i - \mathbf{R}_0| \approx r} - |\omega|r$  we also subtracted the part responsible for the crystallite’s overall solid body rotation to improve the visibility of what can then be interpreted as a tangential shear stress. While the

compression of the cluster by  $F_r$  mostly helps to maintain its crystalline structure, the tangential stress  $F_\phi$  imposes unequal torques on the concentric particle shells, thereby inducing the tangential shear bands and breakup events seen in the phases III-VI. It is noteworthy that, due to the normalization of the nominal velocities  $|\mathbf{F}_i| = 1$ , these two competing tendencies are not independent in our system. Upon increasing the delay time  $\delta t$ , the nominal velocities increasingly tilt away from the central direction, meaning that the pressure decreases while the shear increases, at the same time, aggravating the destabilization. Also, for the non-compact crystallites forming for longer delays, the radial forces themselves may cause radial shear bands and additionally contribute to the breaking of the crystalline configuration.

In the following, we characterize the individual dynamical phases in greater detail. The best intuitive insight into their dynamic nature is gathered from the SV.

I) *Static crystallite*:  $\delta t \lesssim 0.75\rho$ . For short delays  $\delta t$ , the active Brownian particles are propelled exactly toward the target by their nominal velocities, as shown in last two lines of fig. 3 and fig. S1 in the SM. Due to the steric repulsion, they form a non-rotating densely packed hexagonal crystallite (with small Brownian fluctuations). Its radial distribution function  $p(r)$  resembles that of close-packed hard discs, while the dynamical order parameters  $\omega$  and  $\dot{\Gamma}$  vanish.

II) *Spinning crystallite*:  $0.75\rho < \delta t \lesssim 0.94\rho$ . Upon increasing the delay time  $\delta t$  beyond the threshold  $0.75\rho$ , the crystallite exhibits solid body rotation around the target particle. The order parameters thus remain the same as in phase I, with the exception that  $\omega(r) = \omega$  is given by a nonzero constant that is accurately predicted by the single-particle theory. However, as the particles' propulsion speed is fixed to 1, the particles closer to the target would individually prefer to move with larger angular velocities than those further away, while a constant  $\omega(r)$  is enforced by the steric interactions and the radial pressure exerted by the particles in the periphery, which still predominantly aim at the center. These features are nicely reflected in the radial and tangential projections of the nominal velocity in fig. 3 and the nominal velocity field in fig. S1 of the SM. Notice that the nominal tangential velocities of particles near the target/periphery are larger/smaller than  $\omega r$ , which induces the tangential shear stresses that attempt to break up the crystallite.

III) *Quaking crystallite*:  $0.94\rho \lesssim \delta t \lesssim 1.05\rho$ . The tangential shear stresses caused by inhomogeneous angular velocity  $\omega(r)$  grow with increasing time delay. At  $\delta t \approx 0.94\rho$  they overcome the compressive forces and create shear bands. As shown in fig. 3, the inner particles rotate (almost) at the optimal single-particle angular velocity  $\pi/(2\delta t)$ . The periphery lags behind, intermittently detaching and sliding around the rotating core (see the snapshots of the system in figs. 3 and 4, and supplementary video VideoS2.mp4). These stick-slip events cause

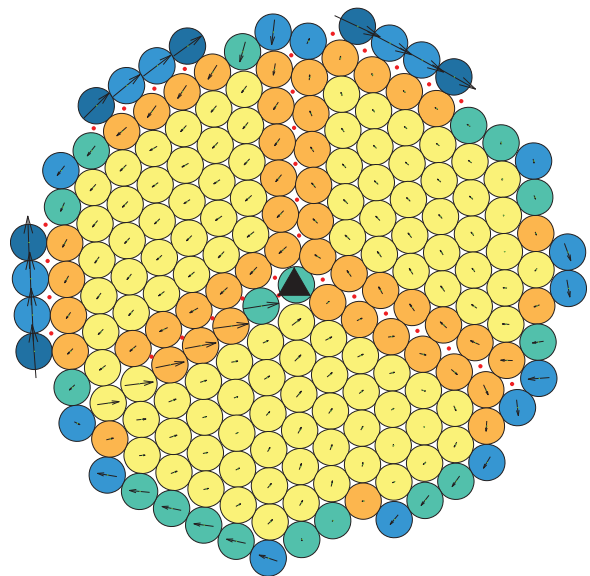


Fig. 4: Snapshot of the supplementary video VideoS3.mp4 ( $\delta t = 7.1$ ,  $N = 199$ , phase III). Particle color codes for the number of nearest neighbors (from 2 to 6: steel blue, sky blue, aquamarine, orange and yellow). Red dots mark shear bands. The arrows show the actual velocities of the particles in the co-moving, co-rotating frame. The black triangle depicts the system's center of mass, which here overlaps with the central target particle. The meanings of the symbols in all SV are the same.

a staircase-like increase of the shear strain  $\Gamma(t)$  (not observed around bulk particles that are not part of a shear band), and can be interpreted as quakes of the outer shell.

The last two rows of fig. 3 and fig. S1 of the SM moreover indicate that the nominal velocities of particles along radial rays from the center are no longer parallel. Closer to the center they have larger tangential components than at the periphery, creating a pressure imbalance in the system. One can interpret this as a result of the tendency of the particles to propel toward the optimal single-particle orbit, which expands with increasing  $\delta t$ , as indicated in the  $p(r)$  panels. Upon increasing the delay somewhat beyond the value  $\delta t \approx 0.94\rho$ , for which the tangential shear bands appear (*e.g.*, from  $\delta t = 7$  to  $\delta t = 7.1$  for  $N = 200$ ), the corresponding pressure imbalance eventually also causes the formation of system-spanning radial shear bands. Once a single radial band is formed, it destabilizes the next neighbor shell around the immobile target particle, which nucleates two more bands by the dilatancy effect, as shown in fig. 4. The angles between the three bands are  $2\pi/3$ , corresponding to three equally sized fragments. Along the shear bands, particles slide in opposite directions (see the SV).

IV) *Ring*:  $1.05\rho \lesssim \delta t \lesssim 1.20\rho$ . The single particle theory predicts that the outermost layer of the crystallite would start to rotate by itself (*i.e.*, even if the rest of the crystallite was fixed), at  $\delta t = \rho$ . Some of the pressure

onto the crystalline core is thereupon released, which facilitates its “breathing” due to the dilatancy effect. The core particles can then follow more freely their tendency to approach the optimal single-particle orbit, thereby creating an outward pressure (fig. S1 in the SM). As a result, the crystallite detaches from the central target particle and forms a ring, in which particles inside and outside the optimal orbit converge toward it. The crystalline structure is then no longer compressed only from the outside but also from the inside. The corresponding stresses increase the frequency of quakes and tangential and radial shear-band formation throughout the ring, as witnessed by  $\Gamma(t)$  (fig. 3). The associated repeated breaking and healing effectively melts the crystalline structure as is reflected in the monotonic decay of the angular velocity  $\omega(r)$  with increasing distance  $r$  from the target and the loss of structure in the radial distribution function. Both effects are somewhat moderated within the fragments forming after the permanent breakup of the ring into the yin-yang shape, described next.

V) *Yin-yang/blobs*:  $1.2\rho \lesssim \delta t \lesssim 2.1\rho$ . The effective contractile force due to the inward-outward pressures described above for the ring structure destabilize the ring in a manner similar to the capillary forces in a Plateau-Rayleigh instability [23]. It therefore tends to break up into  $2\pi l/2l = \pi \approx 3$  equally sized fragments, where  $2l$  is the ring width. Due to the (essentially) athermal conditions, the exact features of the breakup depend on initial conditions, as seen in supplementary videos [VideoS8.mp4](#), [VideoS9.mp4](#), [VideoS10.mp4](#). The contractile forces towards the optimal orbit also causes larger clusters to orbit more slowly than smaller ones. They contain particles further away from the optimal radius, pointing less along the orbital direction. This slows down larger fragments compared to smaller ones, so that smaller fragments will chase the larger ones, thereby giving rise to some coarsening.

One might therefore conclude that the many-body system would ultimately form a giant quasi-particle, centered on the optimal orbit. However, as long as the radius of the closely packed crystallite  $\rho$  is larger than the optimal orbit radius  $R = 2\delta t/\pi$ , such quasi-particle would constantly be damaged by the fixed target particle and therefore actually cannot form. As a result, coarsening is interrupted and the system instead forms a highly dynamical yin-yang structure where the yin part continuously “steals” particles from the yang part, and *vice-versa*. For larger delays, the yin (or the yang) component outgrows its partner until it hits the target particle. The steady state ultimately consists of a single cluster in contact with the target particle, surrounded by several sub-clusters traveling close to the optimal single-particle orbit. Also note that, due to their fixed speed, the particles in the fragments move with larger angular velocities the closer they are to the center (fig. 3). Together with their tendency to propel towards the optimal orbit, this causes a retrograde spinning of the fragments around their own centers of mass. With respect

to the order parameters depicted in fig. 3, the yin-yang phase exhibits the same phenomenology as the ring phase.

To quantify the phase boundaries, we again resort to the bifurcation diagram in fig. 1. It shows that the average angular displacement during one delay time,  $\omega\delta t$ , monotonically increases with  $\delta t$  up to  $\delta t = 0.75\rho\pi/2 \approx 1.18\rho$ , when it saturates at the value  $\omega\delta t = \pi/2$ . This is when a single active particle would detach from the fixed target particle, as its optimal orbit of radius  $R$  takes off. This suggests that the tendency to break the ring and form a single eccentric crystallite, centered on the optimal orbit, would start at  $\delta t > 1.18\rho$ , which is indeed close to the observed value  $1.2\rho$ , and would eventually succeed once the optimal orbit radius  $R$  exceeds  $\rho$ . At this point a spherical crystallite would no longer interfere with fixed target particle at the center. Why this estimate fails to provide the correct condition for the transition to the last dynamical phase is explained in the next paragraph.

VI) *Satellite*:  $\delta t \gtrsim 2.1\rho$ . As pointed out in the preceding paragraph, one would expect to find a single compact satellite orbiting the target particle (roughly) on the optimal single-particle orbit, when  $R \approx \rho$ , hence  $\delta t = \pi\rho/2$ , which is actually not the case. The discrepancy is caused by the fact that the satellite is actually not circular but somewhat elongated along an axis that is slightly tilted relative to the radial direction. The reason is that the pressure exerted by the individual particles is no longer radially symmetric (see fig. S1 in the SM).

The stick-slip motion of particles along the shear bands in this phase is somewhat reminiscent of an extreme version of the terrestrial tides caused by the motion of the Moon around Earth. The major difference is that the tidal forces correspond to an attraction rather than a repulsion relative to the satellite center. As a result, the quake dynamics is approximately out of phase by  $\pi/2$ , with respect to the Moon-Earth system [24] (supplementary video [VideoS6.mp4](#)). Moreover, the attraction does not act toward the satellite center but toward the optimal single-particle orbit. And finally, the elongation of the crystallite is not perfectly aligned with the direction to the center, giving rise to another phase shift that depends on the precise model parameters.

Concerning the order parameters depicted in fig. 3, the satellite phase again exhibits almost the same phenomenology as the ring phase. The only difference is the radial distribution, which is now much broader than in the other five phases. This is indicative of the destructive effect of the tidal quakes, which dynamically dilate and melt the crystallite into an effectively liquid droplet.

**Discussion and conclusions.** – We have numerically studied a two-dimensional ensemble of soft active Brownian particles steered toward a target particle with a time delay. The particles form a closely packed hexagonal crystallite around the target for short delay times and experimentally relevant noise intensities. However, with increasing delay, a much richer behavior is observed. The

average angular velocity around the target exhibits a bifurcation, which can be mapped to the one found recently for a single active particle [1]. An interesting “plastic” deformation of the hexagonal crystalline structure ensues. The tangential and radial shear stresses grow with time delay, eventually creating shear bands and breaking the crystallite. Its overall shape changes with increasing delay from a disc over a ring around the target to a yin-yang and eventually an elongated retrograde spinning satellite orbiting the target.

Our study demonstrates that simple time-delayed interactions can induce very complex dynamical behaviors in many-body systems, even in the case of delayed attractions to a common fixed target. As time delays are omnipresent in interacting active matter systems in nature, this observation should be taken into account when interpreting experimental data. To this end, it would be interesting to realize the studied many-body system experimentally. In this case, hydrodynamic interactions between the active particles would play an important role and potentially give rise to somewhat different results as obtained above, for the idealized active Brownian particle system. Our essentially athermal dynamics might thereupon become more ergodic and fluid-like [21,22,25].

Our results could be extended in several other directions. First, one could consider substantially larger particle numbers than in the present simulations. Our preliminary results suggest that the phase diagram stays essentially the same, while it seems possible to introduce a finer division of phases for short delays. Second, one may consider attraction to a fixed position in space rather than to a fixed target particle. Our preliminary results with this setup reveal two major differences. Firstly, the minimum radius of rotation is determined by the noise, not by the particle diameters. Secondly, omitting the target particle increases the accessible state space. For example, the dynamics in the yin-yang/blobs phase (V) becomes much richer without the central particle, allowing for an almost deterministic periodically switching chirality. Of more practical interest might be the extension of our setup to an all-to-all attraction between the particles. Our preliminary results show that the phenomenology essentially remains unchanged, for short delay times. Differences appear for longer delays, where the emerging patterns are more symmetric compared to what we found above, and would deserve further study. Finally it would be interesting to connect our particle simulations to effective field theories [26].

\*\*\*

We gratefully acknowledge funding through DFG-GACR cooperation by the Deutsche Forschungsgemeinschaft (DFG Project No 432421051) and by the Czech Science Foundation (GACR Project No 20-02955J). VH

additionally acknowledges the support of Charles University through project PRIMUS/22/SCI/009.

*Data availability statement:* The data that support the findings of this study are available upon reasonable request from the authors.

## REFERENCES

- [1] WANG X., CHEN P.-C., KROY K., HOLUBEC V. and CICHOS F., *Nat. Commun.*, **14** (2023) 56.
- [2] BÄUERLE T., LÖFFLER R. C. and BECHINGER C., *Nat. Commun.*, **11** (2020) 2547.
- [3] LÖFFLER R. C., BÄUERLE T., KARDAR M., ROHWER C. M. and BECHINGER C., *EPL*, **134** (2021) 64001.
- [4] BREGULLA A. P., YANG H. and CICHOS F., *ACS Nano*, **8** (2014) 6542.
- [5] SELMKE M., KHADKA U., BREGULLA A. P., CICHOS F. and YANG H., *Phys. Chem. Chem. Phys.*, **20** (2018) 10521.
- [6] BECHHOEFER J., *Rev. Mod. Phys.*, **77** (2005) 783.
- [7] RAMASWAMY S., *J. Stat. Mech.: Theory Exp.*, **2017** (2017) 054002.
- [8] SUN Y., LIN W. and ERBAN R., *Phys. Rev. E*, **90** (2014) 062708.
- [9] GIUGGIOLI L., MCKETTERICK T. J. and HOLDERIED M., *PLOS Comput. Biol.*, **11** (2015) e1004089.
- [10] MIJALIKOV M., MCDANIEL A., WEHR J. and VOLPE G., *Phys. Rev. X*, **6** (2016) 011008.
- [11] LEYMAN M., OGE MARK F., WEHR J. and VOLPE G., *Phys. Rev. E*, **98** (2018) 052606.
- [12] SCHOLZ C., JAHANSHAHI S., LDOV A. and LÖWEN H., *Nat. Commun.*, **9** (2018) 5156.
- [13] KHADKA U., HOLUBEC V., YANG H. and CICHOS F., *Nat. Commun.*, **9** (2018) 3864.
- [14] PIWOWARCZYK R., SELIN M., IHLE T. and VOLPE G., *Phys. Rev. E*, **100** (2019) 012607.
- [15] MUIÑOS-LANDIN S., FISCHER A., HOLUBEC V. and CICHOS F., *Sci. Robot.*, **6** (2021) eabd9285.
- [16] HOLUBEC V., GEISS D., LOOS S. A. M., KROY K. and CICHOS F., *Phys. Rev. Lett.*, **127** (2021) 258001.
- [17] FRÄNZL M., MUIÑOS-LANDIN S., HOLUBEC V. and CICHOS F., *ACS Nano*, **15** (2021) 3434.
- [18] BIALKÉ J., LÖWEN H. and SPECK T., *EPL*, **103** (2013) 30008.
- [19] LHERMINIER S., PLANET R., VEHEL V. L. D., SIMON G., VANEL L., MÅLØY K. J. and RAMOS O., *Phys. Rev. Lett.*, **122** (2019) 218501.
- [20] TSAI J.-C. J., HUANG G.-H. and TSAI C.-E., *Phys. Rev. Lett.*, **126** (2021) 128001.
- [21] SCHALL P. and VAN HECKE M., *Annu. Rev. Fluid Mech.*, **42** (2010) 67.
- [22] WU Y. L., DERKS D., VAN BLAADEREN A. and IMHOF A., *Proc. Natl. Acad. Sci. U.S.A.*, **106** (2009) 10564.
- [23] MEHRABIAN H. and FENG J. J., *J. Fluid Mech.*, **717** (2013) 281.
- [24] HOBBS T., *How Apollo 11’s moonquakes changed our understanding of earthquakes* (Temblor) 2019.
- [25] STEVENS M. J., ROBBINS M. O. and BELAK J. F., *Phys. Rev. Lett.*, **66** (1991) 3004.
- [26] HUANG Z.-F., MENZEL A. M. and LÖWEN H., *Phys. Rev. Lett.*, **125** (2020) 218002.